Modulation of Electrical Conductivity and Lattice Distortions in Bulk HVPE-Grown GaN

Niklas Wolff,[1] Philipp Jordt,[2] Tudor Braniste,[3] Veaceslav Popa,[3] Eduard Monaico, [3]
Veaceslav Ursaki,[3] Adrian Petraru,[4] Rainer Adelung,[5] Bridget M. Murphy,[2,6,z]
Lorenz Kienle,[1,z] and Ion Tiginyanu [3,7,*,z]

[1]*Synthesis and Real Structure, Institute for Materials Science, Kiel University, 24143 Kiel, Germany*
[2]*Institute for Experimental and Applied Physics, Kiel University, 24118 Kiel, Germany*
[3]*National Center for Materials Study and Testing, Technical University of Moldova, MD-2004 Chisinau, Republic of Moldova*
[4]*Nanoelectronics, Institute for Materials Science, Kiel University, 24143 Kiel, Germany*
[5]*Functional Nanomaterials, Institute for Materials Science, Kiel University, 24143 Kiel, Germany*
[6]*Ruprecht-Haensel Laboratory, Kiel University, 24118 Kiel, Germany*
[7]*Academy of Sciences of Moldova, MD-2001 Chisinau, Republic of Moldova*

The nature of self-organized three-dimensional structured architectures with spatially modulated electrical conductivity emerging in the process of hydride vapor phase epitaxial growth of single crystalline n-GaN wafers is revealed by photoelectrochemical etching. The amplitude of the carrier concentration modulation throughout the sample is derived from photoluminescence analysis and the localized heterogeneous piezoelectric response is demonstrated. The formation of such architectures is rationalized based on the generation of V-shaped pits and their subsequent overgrowth in variable direction. Detailed structure analysis with respect to X-ray diffraction and transmission electron microscopy gives striking evidence for inelastic strain to manifest in distortions of the P6$_3$*mc* wurtzite-type structure. The deviation from hexagonal symmetry by angular distortions of the β angle between the basal plane and c-axis is found to be of around 1°. It is concluded that the lattice distortions are generated by the misfit strains originating during crystal growth, which are slightly relaxed upon photoelectrochemical etching.

Over the last 20 years GaN has become one of the most important semiconductor materials and may replace Si in many electronic applications. Particularly, it is already replacing Si in LDMOS radio-frequency devices used in base stations for mobile communication as well as GaAs for radar applications.[1–7] The highly advantageous properties of GaN-based semiconductors such as high electron mobility and saturation velocity, high sheet carrier concentration at heterojunction interfaces, high breakdown field, and low thermal impedance make them extremely promising for high-power high-temperature microwave applications, as evidenced by their high Johnson's figure of merit.[8–10] Exemplary, solid-state lighting optoelectronic devices assembled from white LEDs based on GaN are replacing conventional light sources such as incandescent bulbs and fluorescent lamps nowadays. This is due to their high efficiency, long operational lifetime, compact form factor, no emission of harmful ultraviolet (UV) or infrared radiation, and low maintenance cost. A recent review also highlights the prospects of GaN LEDs for visible light communications (VLC) in both fiber and free-space embodiments.[11] The state-of-the-art technology enabling bandwidth of GaN LEDs in the range of >400 MHz has been explored and multi-gigabit-per-second VLC has been demonstrated.

Better performance characteristics than those of Si power devices make also GaN power devices promising for automotive applications.[12] These electronic applications are based on using primarily silicon or silicon carbide substrates, since from a synthesis point of view thick GaN substrates are commercially unavailable. In spite of considerable progress in addressing the challenges related to significant mismatches between crystal lattices and thermal expansion coefficients, as well as silicon thermal stability when using Si substrates,[13] GaN-on-Si, GaN-on-SiC, and GaN-on-Sapphire remain costly solutions. In fact, GaN remains the most costly electronic material among the wide bandgap compounds (excluding single crystalline diamond).

For a long time, GaN has been grown by Metalorganic Chemical Vapor Deposition (MOCVD) on sapphire, Si, or SiC for research and device applications. However, challenges related to the growth of high-performance films remain, still hampering their utilization in devices.[14] Therefore, single crystalline GaN substrates are essential for future high-performance devices.

Nowadays, there are three main technologies used for GaN crystal growth: hydride vapor phase epitaxy (HVPE), sodium flux, and ammonothermal growth.[15] The last two approaches belong to the group of solution growth methods. High structural quality and high purity have been demonstrated by using the sodium flux growth method. However, it is supposed that this method is a perfect technology for fabricating seeds for further growth of gallium nitride but not for mass production of crystalline wafers, because this technological process is quite expensive and complicated.[15] On the other hand, the ammonothermal growth seems to be appropriate for mass production of GaN crystals, high structural quality substrates with 2-inch diameters and various electrical properties being successfully grown.[16] However, the main problem of this technology is the low growth rate of up to a few micrometers per hour. Apart from that, despite the high crystalline quality, the properties of ammonothermal GaN crystals and substrates are affected by the presence of impurities and other defects that hinder their use for device applications.[17] Therefore, the most appropriate approach for manufacturing GaN substrates is considered HVPE, due to the relatively high growth rate (>100 μm/h) and crystallization of high-purity material.[15] In spite of important advantages of this technology, however, achieving a good crystalline quality is still challenging, because of the formation of V-shaped defects or pits, which lead to the formation of extended inhomogeneous structures upon subsequent overgrowth (see for example Refs. 18,19). Self-organized 3D nanostructured architectures including quasi-ordered concentric hexagonal structures generated during the growth of single crystalline *n*-GaN substrates by HVPE have been revealed by subjecting the samples to electrochemical or photoelectrochemical (PEC) etching.[18] It was supposed that these architectures are produced due to a fine modulation of doping related to the spatial distribution of impurities in the volume of samples generated by some peculiarities of the HVPE growth.

In this paper, we demonstrate by means of transmission electron microscopy (TEM) that the self-organized nanostructured architectures disclosed by photoelectrochemical etching are not related to systematic variations of the crystal structure but by the modulation

---

*Electrochemical Society Member.
zE-mail: murphy@physik.uni-kiel.de; lk@tf.uni-kiel.de;
ion.tighineanu@cnstm.utm.md

of electrical parameters, e.g. by zero and one dimensional defects. Furthermore, we disclose a monoclinic or triclinic lattice distortion of the wurtzite structure by the combination of electron diffraction (ED) and X-ray diffraction (XRD) techniques. We estimate the amplitude of modulation of the free carrier concentration by making use of photoluminescence spectroscopy. The prospects of employing the fine modulation of electrical conductivity for the purpose of nanostructuring by design of GaN and related materials are also discussed. We suggest that the lattice distortion is kinetically induced and measure residual misfit strains of the crystal which relax upon photoelectrochemical etching.

Experimental

The experiments have been realized on 2-inch diameter HVPE-grown n-GaN single crystalline templates acquired from SAINT-GOBAIN Crystals. The 300 μm thick wurtzite-phase GaN substrates were of (0001)-orientation with virgin Ga-face and polished N-face. The density of threading dislocations in the substrates was in the range of $(1-2) \times 10^7$ cm^{-2}. PEC etching was carried out in a stirred 0.1 mol. aqueous solution of KOH for periods up to 30 min under in-situ ultraviolet (UV) illumination provided by focusing the radiation of a 350 W Hg lamp to a spot of about 3.5 mm in diameter on the sample surface. No bias field was applied to the sample during etching, the electrical circuit being closed with a platinum electrode in the electrolyte and an electrical contact made on the back side of the sample using a conductive silver paste. The morphology of as-grown and PEC-etched GaN samples was studied using Zeiss Ultra Plus and VEGA TESCAN TS 5130MM scanning electron microscopes equipped with an INCA Energy 200 EDX System (Oxford Instruments) for chemical composition microanalysis, as well as using a NANOSTATION Atomic Force Microscope (AFM) from Surface Imaging Systems. The local piezoelectric response has been monitored by the piezoresponse force microscopy techniques (PFM) on a SmartSPM 1000 scanning probe microscope from AIST-NT. A sinusoidal modulation voltage of 10 V peak-to-peak at a resonance frequency of 247 kHz was applied between the conductive tip and the sample. The scan was performed in contact mode acquiring the topographic image simultaneously to the vertical piezoresponse amplitude and phase. The photoluminescence (PL) spectra were measured in a temperature interval from 10 to 300 K under excitation by radiation from a He-Cd laser with a wavelength of 325 nm operating in a continuous-wave (CW) mode.

The transmission electron microscopy investigation was carried out on a FEI Tecnai F30 STwin instrument operating at 300 kV (spherical aberration constant $C_S = 1.2$) to determine the structural features of as-grown HVPE single crystalline templates as well as PEC-etched GaN samples using electron diffraction and high-resolution transmission electron microscopy (HRTEM). Electron transparent cross-sectional specimens ($\sim 12 \times 8$ μm) were prepared via a dual beam scanning electron microscope FEI Helios Nanolab system performing a standard focused ion beam (FIB) technique. To account for the high surface roughness and to achieve a more homogenous covering of samples subjected to PEC etching we deposited a layer of carbon using the E-beam prior to the deposition of platinum protection layers to fill up the concentrically etched trenches. For the high-resolution X-ray diffraction (HRXRD) investigations, we used a Rigaku Micromax rotating anode with the characteristic Cu-K$_\alpha$ X-ray energy, at a wavelength of 1.54 Å. The beam size was 1×1 mm^2 ($h \times v$) with a resolution of 2×10^{-4} Å^{-1}.

Results and Discussion

SEM images demonstrate some quasi-periodical modulation of the physical properties of as-grown HVPE samples both on the top surface (Figure 1a, upper part) and in the bulk (a cross-sectional view is illustrated in the lower part of Figure 1a). We suggest that these features are related to the modulation of the electrical conductivity across the sample volume, as SEM is sensitive to electrical parameters of the ma-
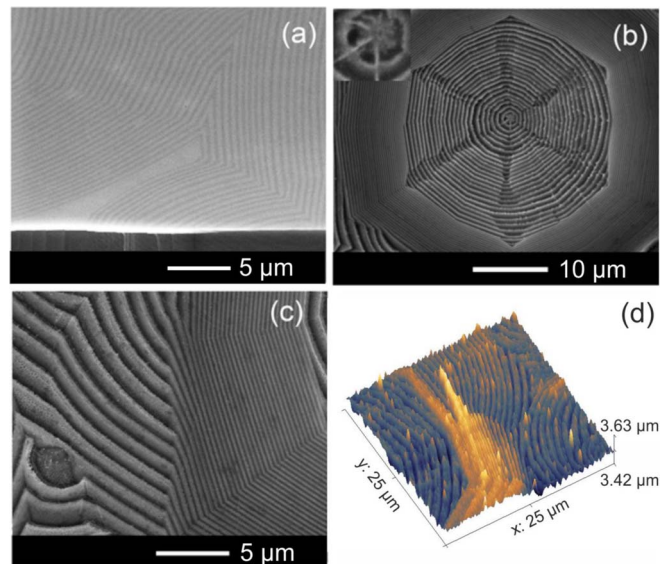

Figure 1. Oblique SEM view (a) of a cleaved as-grown HVPE GaN sample revealing an alternating bright-dark pattern. SEM (b,c) and AFM (d) images of nanostructured regions showing the micrometer deep etched trenches produced in a HVPE GaN sample subjected to PEC etching.

terial. A model describing the occurrence of such modulations during the HVPE crystal growth has been proposed previously.[18,19]

The morphology of a GaN sample subjected to PEC etching as revealed by SEM and AFM is illustrated in Figures 1b–1d which discloses concentric rings forming hexagonal patterned domains on the surface of the sample with the average density of approximately 10^4 cm^{-2}. In PEC etched samples, the pattern in SEM images arises due to differences in the rates of electrochemical dissolution of regions exhibiting different values of electrical conductivity, while in as-grown samples the light-dark pattern is caused by the modulation of the electrical conductivity. So, PEC etching proves to be a versatile tool for disclosing patterns of electrical parameters in inhomogeneous semiconductors. One can see from Figure 1b that the formation of nanostructured domains starts at certain points at early stages of the crystal growth, and these domains develop further according to the previously proposed model.[18] The insert in Figure 1b suggests that these nucleation points are genetically related to sites with a high density of dislocations, which are evidenced by PEC etching, since it is well established that the dislocations in GaN are resistant against PEC attack.[20–22] The morphology of regions where differently nanostructured domains intersect each other is illustrated in Figures 1c, 1d. The 3D spatial architecture of these porous domains can be described as hollow cones which are concentrically stacked into each other as exemplified in Figure S1 (Supplementary Information) by a SEM image taken from an electrochemically etched sample.

Note that there is a difference in the mechanisms of electrochemical and PEC etching of GaN. In an electrochemical process, the regions possessing higher electrical conductivity usually are characterized by a higher degree of porosity. In contrast to that, the etch rate during PEC etching decreases linearly with the logarithm of the carrier concentration, i.e. the regions with lower carrier concentration are etched faster than surrounding regions, which leads to the formation of concentric rings along the surface subjected to etching.[22] Further images of the photoelectrochemically etched GaN surface can be found in Figure S2, illustrating the clear modulation of electrical conductivity.

An interesting issue is the estimation of the amplitude of modulation of electrical parameters across the material as a result of peculiarities of the HVPE growth. Qualitative PFM measurements revealed a modulation of the local piezoresponse within hexagonal patterned domains and boundary regions in between, further named "islands", a phenomenon which can be correlated with the presence of inversion
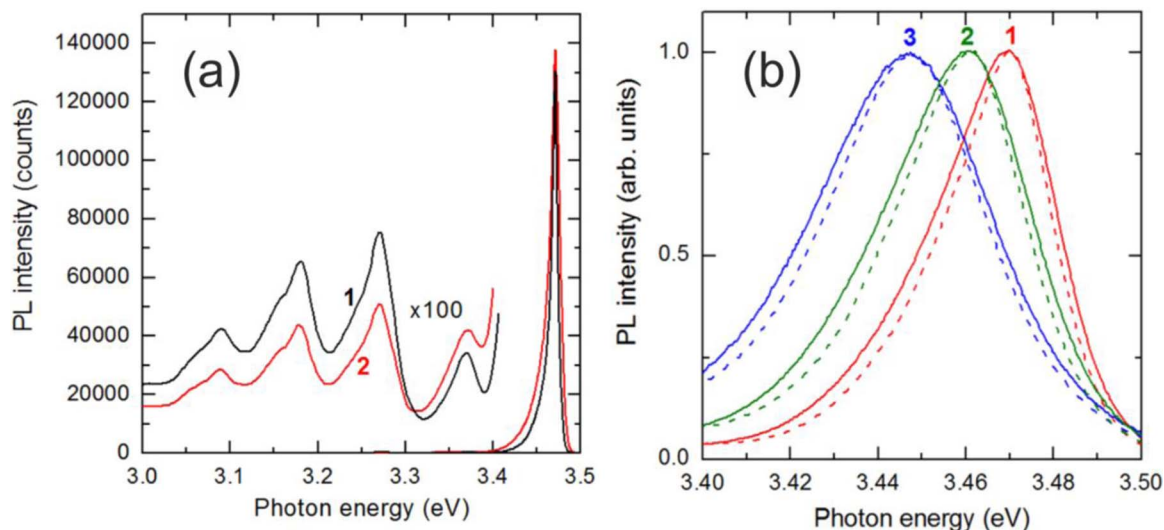
Figure 2. (a) PL spectrum of as-grown (curve 1) and PEC etched (curve 2) GaN samples measured at 10 K. (b) The NBG PL band measured at 75 K (curves 1), 100 K (curves 2), and 150 K (curves 3) in the as-grown (dashed line) and PEC etched (solid line) samples.

domains.[23] The results are presented and discussed in Figure S3. Further, in a previous study by means of Kelvin Probe Force Microscopy,[18] it was suggested that the fine modulation of doping is related to the spatial distribution of impurities. It is difficult, however, to estimate the amplitude of modulation by means of this methodology. In this paper, we make use of PL spectroscopy for the purpose of evaluating the amplitude of spatial modulation of the free carrier concentration in the specimen.

According to a semi-classical model regarding the broadening of impurity bands in heavily doped semiconductors developed by Morgan,[24] the carrier concentration can be estimated from the dependence of the photoluminescence full width at half maximum (FWHM) on the carrier concentration. This model has been previously applied to explain the broadening of near-band-gap (NBG) photoluminescence in *n*-GaN films.[25] It was shown that the model can be reliably applied to GaN samples with an electron concentration higher than 10^{18} cm^{-3}, and a calibration curve has been deduced for the relation between the FWHM of the NBG photoluminescence measured at 77 K and the electron concentration in the GaN material.

The PL spectra measured at 10 K for both the as-grown and the PEC etched samples (Figure 2a) are typical for GaN according to samples grown previously by using various techniques. Apart from the NBG PL band with the maximum at 3.471 eV, a series of PL bands with an intensity more than two orders of magnitude lower are observed in the spectral range from 3.0 to 3.4 eV. Note also the presence of a broad green PL band with nearly the same intensity in the visible spectral range (not shown in this figure). The band located at 3.37 eV could be attributed to a free-to-bound transition, while several bands in the spectral range of $3.2 - 3.3$ eV followed by one- and two-phonon replicas are usually associated with donor-acceptor pair (DAP) transitions.[26,27] The origin of the 3.27 eV PL band as a DAP recombination has been well documented in the literature through its shift to higher photon energies with increasing the excitation power density and a transition from a DAP recombination to conduction band-acceptor recombination at an elevated temperature. The PL band at 3.27 eV with two shoulders at 3.29 eV and 3.24 eV suggests the presence of different impurities in our samples. However, additional investigations are needed to identify the chemical nature of the respective impurities.

The analysis of the NBG PL band (Figure 2b) discloses its slight broadening in the PEC etched sample as compared to the as-grown one: the FWHM increases from 29 to 33 meV at 75 K, from 35 to 40 meV at 100 K, and from 42 to 47 meV at 150 K. By using the calibration curve from Ref. 25, one can estimate that at 75 K the carrier concentration increases from 1.0×10^{18} cm^{-3} in the as-grown sample to 1.6×10^{18} cm^{-3} in the PEC etched sample, i.e. the carrier concentration

increases by ca. 60%. These data corroborate the previous findings that PEC etching removes basically the material with low conductivity and leaves areas with higher carrier concentration. On the other hand, the as-grown material contains nanorings with both low and high carrier concentration, i.e. the NBG PL band comes as a superposition of a narrow band from rings with low carrier concentration and a broader band from rings with higher carrier concentration. This means that the NBG PL band from areas with low carrier concentration should be even narrower, which would give a carrier concentration lower than the deduced value of 1.0×10^{18} cm^{-3}. In this context, it is clear that the amplitude of modulation of the electrical conductivity in the HVPE samples is even higher than 60%.

The results of TEM investigations show that the self-organized nanostructured electrical architectures produced during HVPE growth seem not to be related to regions of structural variation with respect to a single crystal material. Moreover, the comparison of the as-grown and PEC-etched samples demonstrates a high density of defects such as stacking faults and dislocations close to the surface serving as possible attack sites for the PEC-etch. For the as-grown (0001) nanostructured GaN (see Figures 3a, 3b) dislocation networks originating at the (0001) GaN surface have been observed to extend 200–300 nm deep into the crystal. For the etched sample, a TEM lamella has been cut from the center of the circular formations. Dislocation networks were evidenced to be concentrated at the center of these hexagonal domains, developing along the polar direction throughout the prepared crystal lamella (Figures 3d, 3e). This observation is in congruence to previous investigations of pits at the center of the nanostructured architectures which are related to pile up of screw or mixed-type dislocations using AFM.[18] These defects were visualized by exploiting the diffraction contrast in the scanning TEM (STEM) high-angle annular dark-field mode after tilting away from the [2-1-10] diffraction condition of the crystal to enhance electron scattering processes at defects. Further, we report that after etching, neither dislocation networks nor stacking faults could be observed beneath the (0001) surface, indicating that defect rich regions of the crystal lattice have been preferentially under attack by the PEC-etch, which is especially active for regions with low carrier concentration. Indeed, several reports exist about the influence of crystal defects in GaN on the electric conductivity[27] especially related to threading dislocations and gallium vacancies by e.g. the existence of deep level trapping states[28] in the yellow luminescence band, the reduction of the minority carrier concentration at dislocations acting as non-radiative recombination centers[29] and low transverse mobility by scattering of electrons at charged dislocation lines.[30] However, the dislocation network observed at the center of nanostructured architectures has not been subjected to the
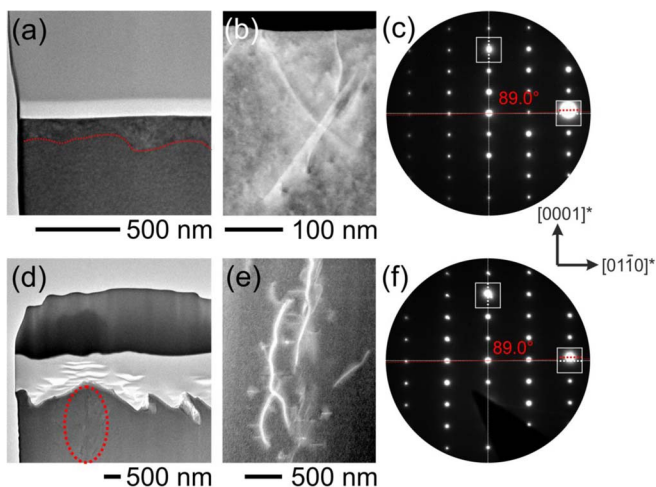
Figure 3. TEM cross-section investigation of the as-grown (a-c) and PEC etched GaN bulk films (d-f). (a) As-grown GaN films show low surface roughness. The red line indicates a change in contrast between the upper and lower part of the crystal, which is related to a high density of near-surface defects such as stacking faults and threading dislocations as depicted in the STEM image in (b). (c) Selected area electron diffraction pattern in [2-1-10] zone axis showing the *c*-axis oriented film growth and a distortion of the reciprocal $\beta \approx 89°$ angle of the wurtzite-type crystal structure ($\alpha° = \beta° = 90°$). (d) Surface etched GaN crystal cut through the center of one hexagonal microdomain (marked with the red ellipse), where dislocation networks were observed in the STEM mode (e). (f) SAED pattern showing the deviation of the reciprocal β angle. The red dashed lines display the angular deviation of the intensities with respect to 90°, white dashed line.

PEC attack as evidenced by the STEM images and described in literature.[20]

The mediation of stress due to crystal lattice mismatch and differences in the thermal lattice expansion coefficients during growth introduce high defect densities of the family of screw, edge, and mixed-type dislocations and have been shown to be concentrated at the substrate/film interface of ~6 mm thick HVPE grown GaN crystals, decreasing in density with the growth direction.[31] Strategies to reduce the generation of high defect densities comprise the initiation of cracks in the sapphire substrate and homoepitaxial growth onto thin GaN seed layers.[32] However, with substantial thickness the large stresses generated lead to the self-separation of substrate and film and could manifest in lattice distortions.[33,34] The results of crystal structure investigations disclose a clear deviation from the $P6_3mc$ wurtzite-type structure in the as-grown and PEC etched samples. A detailed electron diffraction (SAED) study from multiple selected areas revealed a slight deviation of the reciprocal unit-cell angle $\beta \approx 89°$ from rectangularity. The angle β is observed between the [0001]* and [01-10]* directions in the [2-1-10] zone axis pattern (we refer to the magnified insets, in which the red dashed lines display the angular deviation of the intensities with respect to 90°, white dashed line), as depicted in Figures 3c, 3f. The lattice distortion was observed in several selected areas as evidenced from SAED experiments on the as-grown GaN sample (Figure S4). The reduction of symmetry was apparent irrespective of the slight bending of the lamella itself indicated by the increasing amount of out-of-zone axis orientation when moving from i) to iv) in Figure S4(a). Whereas SAED collects more averaged information from a relatively large sample area of $0.785 \,\mu m^2$ in this experiment, the β distortion was also locally observed at the nanoscale by high resolution imaging. HRTEM micrographs and their Fast Fourier Transforms (FFTs) (see Figure 4) taken from different areas of the patterned PEC etched sample show the defect-free nanostructures of the hillocks depicted in Figure 3d. Whereas the analysis of this selected area by FFT (Figures 4a, 4b) does not show any deviation from the 90° angle an even larger distortion of 88° could be observed in neighboring areas (see Figures 4c, 4d). This finding indicates local lattice relaxation potentially due to the increase in free surface upon etching. The variation of the reciprocal angle according to the bulk wurtzite unit cell alters the angle β between the basal plane and the *c* axis. This angular distortion from 90° depending on the direction and the magnitude of strain results in a symmetry reduction in respect to the wurtzite aristotype. The symmetry of the deformed structure may be assigned to a maximum subgroup of $P6_3mc$, e.g. with monoclinic (C*m*11 or C*1c*1) or triclinic symmetry. Due to missing superstructure reflections in the diffraction patterns, the symmetry reduction has to be assigned to as the t-type[35] (for *translationengleich*).

Indeed, structural distortions of $\beta \approx 89.05°$ have been described by Rao et al. as triclinic lattice distortion in wurtzite-type gallium nitride films grown by metal organic vapor-phase epitaxy on sapphire substrates.[36] There, a triclinic distortion was investigated by electron diffraction studies using convergent beam electron diffraction (CBED) and SAED near the film/substrate interface. The large misfit strain during crystal growth was reasoned to be the origin for the lattice distortion and was observed to relax within 1 μm distance from the substrate interface.

In case of rapid growth conditions of a few hundred $\mu m/h$ present in HVPE it seems apparent that the large film stresses due to the initial substrate/film misfit strain can introduce lattice distortions which are then unable to relax in the limited amount of time. Since the lamellae observed in TEM only represent a small fraction of the entire sample volume, high-resolution X-ray diffraction has been applied as a complimentary technique to TEM to probe a larger volume of the sample. This offers quantitative information about the average bulk-like 3D lattice structure and residual strains in the sample with very high resolution.

The experimental setup of the high-resolution X-ray diffraction experiments is depicted schematically in Figure 5a displaying the 2*theta (2θ) measurement geometry. The β-distortion observed in the TEM was tracked down by measuring the angle omega ω, which is the equivalent deviation parameter between the *c*-axis and the surface normal, $\omega = 90° - \beta$. Here, the two examples of a single crystal with a $P6_3mc$ wurtzite-type structure with perfect $\omega = 0$ geometry and a lattice distortion $\omega > 0$ are presented. This offset angle ω is measured by performing rocking scans at several azimuthal positions achieved by a rotation (phi φ) horizontal to the surface normal and monitoring
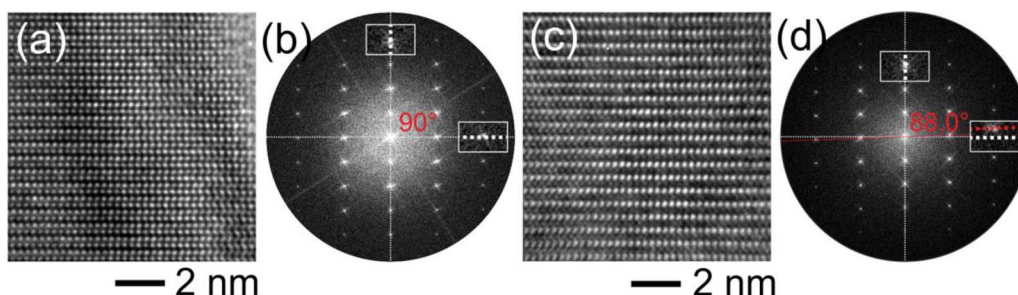

Figure 4. Local high resolution TEM study with corresponding FFT images on PEC etched samples showing areas with apparently no lattice distortion $\beta = 90°$ (a-b) and a stronger distortion of the crystal metrics $\beta = 88°$ (c-d) in GaN films.

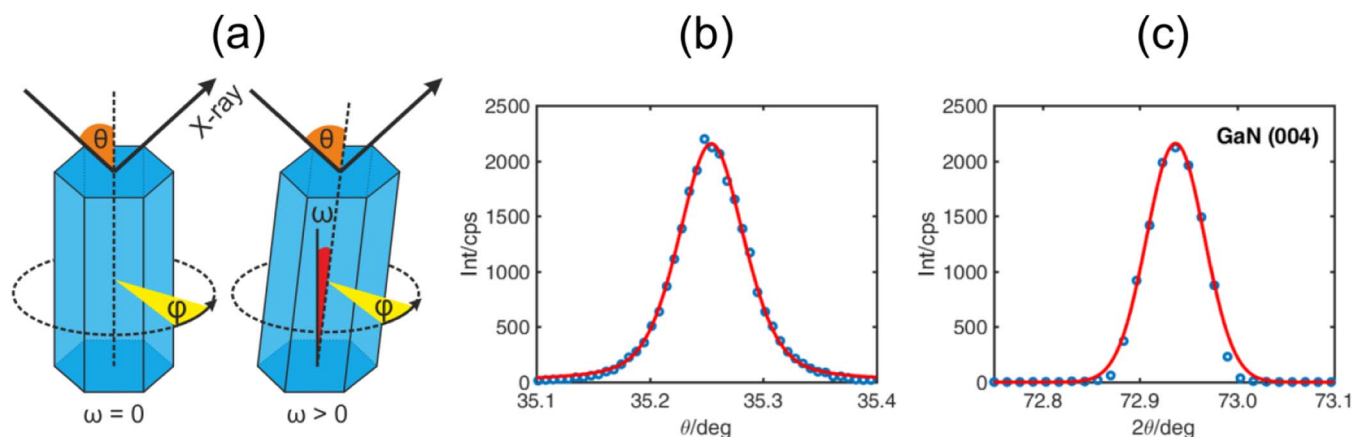**Figure 5.** (a) HRXRD measurement geometry for a hexagonal crystal first showing no triclinic lattice distortion $\omega = 90°\text{-}\beta = 0$ and second with $\omega > 0$ measured in dependence of the sample horizontal rotation angle phi φ in a 2*theta, 2θ, geometry. The single crystalline structure of the as-grown GaN crystal is demonstrated by representative rocking curves (b) and Bragg scans (c) of the (004) reflection, where lattice strains can be derived from peak fits (red curve).

the $Q(\theta)$-shift in the maximum peak intensity of the GaN (004) Bragg reflection, Q being the reciprocal lattice vector.

The position of the GaN (004) Bragg reflection was determined to be $2\theta = 72.935°$ and $Q = 4.85$ Å^{-1}, in agreement with the wurtzite-type structure[37] (a = 3.190Å, c = 5.189Å). The respective rocking curve, performed for optimizing the incident angle θ and the 2θ-scan of the GaN (004) reflection is shown in Figures 5b and 5c, respectively. The blue dotted data points were fitted by Voigt-profiles (red curve) with the contribution (Gauss 40%, Lorentzian 60%) to obtain the peak position and full-width at half maxima which are used to derive lattice strains along the crystal c-axis.

For the analysis of the deviation parameter ω representing the triclinic lattice distortion, rocking curves were performed at nine azimuthal rotation angles φ in steps of 30° for the as-grown and etched samples and were evaluated for their intensity maxima peak position as presented in Figure 6a. Both samples show coinciding angular dependence, which is apparent by the superposition of the measurement curves aligning the $\omega = 0$ data points. The deviation of ω with respect to the in-plane orientation is observed to oscillate between $-1°$ and $1°$ over the measured range having their maxima separated by a 180° rotation in φ which indicates similar results to the lattice distortion $\beta = 89°$ observed with TEM. The respective values of the distortion measured for the as-grown and etched sample at $\phi = 30°$ and $\phi = 210°$ are $\omega_{\text{as-grown}} = 0.9585°$ and $\omega_{\text{etched}} = 0.9917°$, and $\omega_{\text{as-grown}} = -1.0356°$ and $\omega_{\text{etched}} = -1.0360°$, respectively. Therefore an average distortion of $\omega_{\text{as-grown}} = 0.9971°$ and $\omega_{\text{etched}} = 1.0139°$ can be derived for

both samples, indeed indicating a structural phenomenon on the larger length scale, which can be described by a triclinic lattice distortion.

Furthermore, lattice strain can be derived from the total reflection position $Q_{(004)}$ and can be resolved with very high precision of up to 10^{-5}, which provides a significant advantage over other methods of evaluating strain. The variation in the $Q_{(004)}$ value is plotted in Figure 6b for the as-grown and etched GaN samples in dependence of the rotation angle φ. The average Q values have been determined to $Q_{\text{as-grown}} = 4.8502 \pm 0.0001$ Å^{-1} and $Q_{\text{etched}} = 4.8493 \pm 0.0006$ Å^{-1} ($c_{\text{as-grown}} = 5.1818 \pm 0.0001$ Å and $c_{\text{etched}} = 5.1828 \pm 0.0006$ Å) which translates into a compressive strain of $\varepsilon_{\text{as-grown}} = -0.118\%$ and $\varepsilon_{\text{etched}} = -0.101\%$ with respect to the literature value of $Q_{(004)} = 4.8444$ Å^{-1} ($c_{(004)} = 5.189$ Å).[37] The presence of residual compressive stress in free standing HVPE grown bulk GaN substrates has been observed before by various techniques such as micro-reflectance spectroscopy,[38,39] HRXRD and photoluminescence spectroscopy.[40] However, the amount of residual compressive strain on the c-axis reported in these studies is significantly smaller (by one order of magnitude) compared to this work. This discrepancy could possibly be explained by the triclinic lattice distortion observed in this work, reasoned by different crystal growth parameters, crystal thickness, and the choice of substrate or intermediate layers to reduce interfacial stresses. Furthermore, electron diffraction experiments by Rao et al. reporting about the triclinic distortion in 4.5 μm thick MOVPE GaN films on sapphire showed a tensile strained c lattice parameter by about 0.2%, which is at least in the same order of magnitude.[36] For the bulk-like GaN films investigated
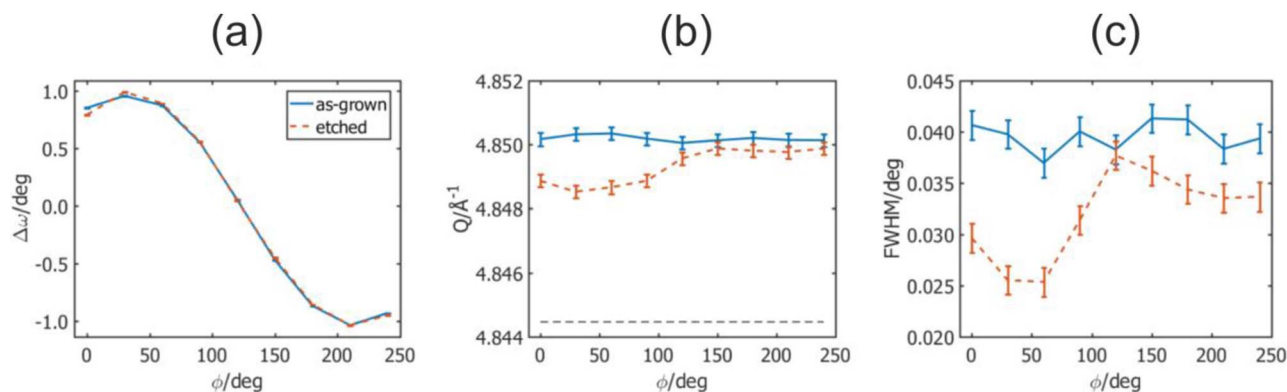

Figure 6. (a) Variation of the deviation parameter omega $\Delta\omega$ in dependence of the rotation angle phi φ from HRXRD. The measurements are showing congruent behavior in the boundaries of $-1°$ to $1°$ for the as-grown and etched samples. (b) Compressive strain $\varepsilon_{\text{as-grown}} = -0.118\%$ and $\varepsilon_{\text{etched}} = -0.101\%$ with respect to the Reference 37 (black dashed line). (c) Full-width at half maximum values of fitted Bragg scans in dependence of the azimuthal rotation. The slightly smaller FHWM width of the etched sample indicates larger coherently diffracted domains which could be attributed to the reduction of defect density after etching.

in this work, the determination of strain from ED pattern, however, seems not to be representative since the information gathered only pictures the first few micrometers and with lower strain precision of just 10^{-3}.

To conclude, next to a monoclinic or triclinic lattice distortion, the amount of residual strain in the HVPE grown crystal was determined by HRXRD to be compressive in *c*-axis direction by about 0.1% for both, the as-grown and etched sample, which slightly tends to relax for the latter.

In Figure 6c the FWHM calculated from the Voigt fits of the Bragg scans is plotted over the azimuthal rotation φ. The mean value of the FWHM is $0.0395 \pm 0.0015°$ for the as-grown and $0.0319 \pm 0.0044°$ for the etched GaN. From the FWHM the size of the coherently diffracting domains can be derived which serves as an indicator for the defect density.[41,42] For the as-grown and etched GaN the mean domain sizes are determined to 111.7 ± 4.3 nm and 140.7 ± 20.8 nm, respectively. In conclusion, the etching process slightly increases the sizes of the coherently diffracting domains, which can be attributed to a reduction in the defect density after etching as evidenced from TEM experiments.

Conclusions

The results of this study demonstrate that the complex 3D nanoarchitectures disclosed by photoelectrochemical etching in HVPE-grown bulk GaN single crystals originate from the spatially modulated electrical conductivity and they prove not to be related to variations of the crystal structure. According to the analysis of the photoluminescence in as-grown and PEC etched samples, the amplitude of spatial modulation of the electrical conductivity in the HVPE-grown GaN is of at least 60%. On the other hand, combining TEM and HRXRD techniques provides a powerful methodological approach to gather structural information on the nanometer to millimeter length scale with high precision. These investigations reveal a distortion of the $P6_3mc$ wurtzite-type structure, indicated by the deviation from the hexagonal symmetry. This deviation varies from 0º to 2º at the nanoscale, while it is of around 1º when averaged over the entire crystal. Furthermore, compressive lattice strain along the crystal *c*-axis derived from peak fits of rocking curves of the (004) reflection is found to be in the order of -0.1% and to be slightly relaxed in PEC-etched samples.

Acknowledgments

Appendix

Further SEM images showing the GaN surface after subjection to electrochemical and photoelectrochemical etching (S1, S2). Discussion of Piezoforce Microscopy results (S3) and electron diffraction pattern conducted on different positions of the specimen (S4).

ORCID

Eduard Monaico https://orcid.org/0000-0003-3293-8645
Ion Tiginyanu https://orcid.org/0000-0003-0893-0854

References

1. P. Waltereit, W. Bronner, R. Quay, M. Dammann, M. Cäsar, S. Müller, F. Van Raay, R. Kiefer, P. Brückner, J. Kühn, M. Musser, L. Kirste, C. Haupt, W. Pletschen, T. Lim, R. Aidam, M. Mikulla, and O. Ambacher, *Phys. Status Solidi Appl. Mater. Sci.*, **209**, 491 (2012).
2. S. Maroldt, R. Quay, P. Dennler, D. Schwantuschke, M. Musser, M. Dammann, R. Aidam, P. Waltereit, A. Tessmann, and O. Ambacher, *Jpn. J. Appl. Phys.*, **52**, 08JN13 (2013).
3. P. Waltereit, W. Bronner, P. Brückner, M. Dammann, R. Reiner, S. Müller, J. Kühn, M. Musser, R. Quay, M. Mikulla, and O. Ambacher, in: *Int. Conf. Solid State Devices Mater.*, 958 (2013).
4. D. Koyama, A. Barsegyan, and J. Walker, in: *2015 IEEE Int. Conf. Microwaves, Commun. Antennas Electron. Syst.*, (2015).
5. R. Lerner, S. Eisenbrandt, C. Bower, S. Bonafede, A. Fecioru, R. Reiner, and P. Waltereit, in: *Proc. Int. Symp. Power Semicond. Devices ICs*, 451 (2016).
6. P. Waltereit, W. Bronner, R. Quay, M. Dammann, M. Cäsar, S. Müller, R. Reiner, P. Brückner, R. Kiefer, F. Van Raay, J. Kühn, M. Musser, C. Haupt, M. Mikulla, and O. Ambacher, *Semicond. Sci. Technol.*, **28**, 074010 (2013).
7. U. K. Mishra and M. Guidry, in: *Power GaN Devices, Power*, Elec M. Meneghini, G. Meneghesso, and E. Zanoni, (Eds.), p.69, Springer, Switzerland, (2017).
8. M. Shur and R. F. Davis, in: *Sel. Top. Electron. Syst*, Vol. 33, M. Suhr, Editor, World Scientific, (2004).
9. J. L. B. Walker, *Handbook of RF and Microwave Power Amplifiers*, Cambridge University Press, Cambridge (2011).
10. R. S. Pengelly, S. M. Wood, J. W. Milligan, S. T. Sheppard, and W. L. Pribble, *IEEE Trans. Microw. Theory Tech.*, **60**, 1764 (2012).
11. S. Rajbhandari, J. J. D. McKendry, J. Herrnsdorf, H. Chun, G. Faulkner, H. Haas, I. M. Watson, D. O'Brien, and M. D. Dawson, *Semicond. Sci. Technol.*, **32**, 023001 (2017).
12. T. Kachi, *Jpn. J. Appl. Phys.*, **53**, 100210 (2014).
13. E. L. Piner, *ECS Trans.*, **77**, 95 (2017).
14. S. Keller, H. Li, M. Laurent, Y. Hu, N. Pfaff, J. Lu, D. F. Brown, N. A. Fichtenbaum, J. S. Speck, S. P. Denbaars, and U. K. Mishra, *Semicond. Sci. Technol.*, **29**, 113001 (2014).
15. M. Bockowski, M. Iwinska, M. Amilusik, M. Fijalkowski, B. Lucznik, and T. Sochacki, *Semicond. Sci. Technol.*, **31**, 093002 (2016).
16. R. Doradziński, R. Dwiliński, J. Garczyński, L. P. Sierzputowski, and Y. Kanbara, in: *Technology of Gallium Nitride Crystal Growth*, D. Ehrentraut, E. Meissner, and M. Bockowski, Editors, p. 326, Springer Berlin Heidelberg (2010).
17. S. Suihkonen, S. Pimputkar, S. Sintonen, and F. Tuomisto, *Adv. Electron. Mater.*, **3**, 1600496 (2017).
18. I. Tiginyanu, M. A. Stevens-Kalceff, A. Sarua, T. Braniste, E. Monaico, V. Popa, H. D. Andrade, J. O. Thomas, S. Raevschi, K. Schulte, and R. Adelung, *ECS J. Solid State Sci. Technol.*, **5**(5), P218 (2016).
19. W. Lee, H. J. Lee, S. H. Park, K. Watanabe, K. Kumagai, T. Yao, J. H. Chang, and T. Sekiguchi, *J. Cryst. Growth.*, **351**, 83 (2012).
20. C. Díaz-Guerra, J. Piqueras, V. Popa, A. Cojocaru, and I. M. Tiginyanu, *Appl. Phys. Lett.*, **86**, 1 (2005).
21. V. Popa, I. M. Tiginyanu, V. V. Ursaki, O. Volcius, and H. Morkoç, *Semicond. Sci. Technol.*, **21**, 1518 (2006).
22. R. Lewandowska, J. L. Weyher, J. J. Kelly, L. Konczewicz, and B. Lucznik, *J. Cryst. Growth*, **307**, 298 (2007).
23. B. J. Rodriguez, A. Gruverman, A. I. Kingon, and R. J. Nemanich, *J. Cryst. Growth*, **246**, 252 (2002).
24. T. N. Morgan, *Phys. Rev.*, **139**, A343 (1965).
25. E. Iliopoulos, D. Doppalapudi, H. M. Ng, and T. D. Moustakas, *Appl. Phys. Lett.*, **73**, 375 (1998).
26. R. Dingle and M. Ilegems, *Solid State Commun.*, **9**, 175 (1971).
27. T. Paskova, B. Arnaudov, P. P. Paskov, E. M. Goldys, S. Hautakangas, K. Saarinen, U. Södervall, and B. Monemar, *J. Appl. Phys.*, **98**, 033508 (2005).
28. P. Kozodoy, J. P. Ibbetson, H. Marchand, P. T. Fini, S. Keller, J. S. Speck, S. P. DenBaars, and U. K. Mishra, *Appl. Phys. Lett.*, **73**, 975 (1998).
29. J. Elsner and R. Jones, *Phys. Rev. B - Condens. Matter Mater. Phys.*, **58**, 12571 (1998).
30. S. J. Rosner, E. C. Carr, M. J. Ludowise, G. Girolami, and H. I. Erikson, *Appl. Phys. Lett.*, **70**, 420 (1997).
31. K. Fujito, S. Kubo, H. Nagaoka, T. Mochizuki, H. Namita, and S. Nagao, *J. Cryst. Growth.*, **311**, 3011 (2009).
32. S. T. Kim, Y. J. Lee, D. C. Moon, C. H. Hong, and T. K. Yoo, *J. Cryst. Growth.*, **194**, 37 (1998).
33. B. H. Bairamov, O. Gürdal, A. Botchkarev, H. Morkoç, G. Irmer, and J. Monecke, *Phys. Rev. B.*, **60**, 16741 (1999).
34. A. Vailionis, H. Boschker, W. Siemons, E. P. Houwman, D. H. A. Blank, G. Rijnders, and G. Koster, *Phys. Rev. B.*, **83**, 064101 (2011).
35. Wiley: *International Tables for Crystallography*, Volume A, 5th Edition, Space-Group Symmetry - Theo Hahn, n.d.
36. D. V. Sridhara Rao, K. McLaughlin, M. J. Kappers, and C. J. Humphreys, *Ultramicroscopy*, **109**, 1250 (2009).
37. H. Schulz and K. H. Thiemann, *Solid State Commun.*, **23**, 815 (1977).
38. H. Geng, H. Sunakawa, N. Sumi, K. Yamamoto, A. Atsushi Yamaguchi, and A. Usui, *J. Cryst. Growth*, **350**, 44 (2012).
39. H. Geng, A. A. Yamaguchi, H. Sunakawa, N. Sumi, K. Yamamoto, and A. Usui, *Jpn. J. Appl. Phys.*, **50**, 01AC01 (2011).
40. V. Darakchieva, T. Paskova, P. P. Paskov, B. Monemar, N. Ashkenov, and M. Schubert, *Phys. Status Solidi*, **195**, 516 (2003).
41. B. Heying, X. H. Wu, S. Keller, Y. Li, D. Kapolnek, B. P. Keller, S. P. DenBaars, and J. S. Speck, *Appl. Phys. Lett.*, **68**, 643 (1996).
42. H. Heinke, V. Kirchner, S. Einfeldt, and D. Hommel, *Appl. Phys. Lett.*, **77**, 2145 (2000).